Available online at www.sciencedirect.com
SCIENCE DIRECT®
Ultramicroscopy 98 (2004) 271–281
ultramicroscopy
www.elsevier.com/locate/ultramic

Lorentz phase microscopy of magnetic materials

V.V. Volkov*, Y. Zhu

Materials Science Department, Brookhaven National Laboratory, Upton, NY 11973, USA

Received 26 March 2003; received in revised form 3 July 2003

Abstract

We propose a method of Lorentz phase microscopy for in situ studies and imaging magnetic materials in transmission electron microscopy (TEM) based on the solution of the magnetic transport-of-intensity equation. We also describe the appropriate way of solving this equation that may be useful for understanding and practical use of non-holographic methods for phase retrieval in electron microscopy, especially in imaging magnetic materials. The method is simple, since it is primarily based on classical Fresnel imaging. On the other hand, it is quantitative and can be applied in any TEM without changing the basic hardware. Therefore, it may well find important practical applications in ultramicroscopy and modern magnetic materials research.

PACS: 42.30.Rx; 75.60.Ch; 07.78.+s

Keywords: Exit wave reconstruction; Phase retrieval; Magnetic imaging; Image processing

1. Introduction

Since the early sixties, Lorentz imaging in transmission electron microscopy (TEM), recorded in Fresnel mode, has been known as a simple classical method to image magnetic materials. Its value in the analysis of domain walls in magnetic materials has been well documented, for example, by Hirsch et al. [1]. Experimentally, the contrast from domain walls is observed when the TEM image is recorded at small defocus, provided that the sample is not magnetically saturated. This implies that the TEM's objective lens must either be switched off or little exited. Unfortunately, this straightforward approach does not yield information on the local magnetization within domains in crystalline magnets and/or magnetization ripple in magnetic foils and films. Therefore, it was never considered as a quantitative method to analyze the domain structure itself. On the other hand, Foucault imaging can be more helpful for visualizing the magnetic domain structure, although the results are more qualitative and very sensitive to the exact position of the objective aperture. To overcome these limitations the new methods for imaging magnetic domains at different length scales have been developed, such as differential phase contrast (DPC) microscopy [2], the magneto-optic Faraday and Kerr effects (MOKE) [3], magnetic force microscopy (MFM) [4], off-axis electron holography [5], scanning electron microscopy with polarization analysis (SEMPA) [6], and

*Corresponding author. Tel.: +1-631-344-7355; fax: +1-631-344-4071.
E-mail address: volkov@bnl.gov (V.V. Volkov).

0304-3991/$ - see front matter © 2003 Elsevier B.V. All rights reserved.
doi:10.1016/j.ultramic.2003.08.026

magnetic circular dichroism [7]. Not all of these methods can display a domain structure at nanoscale resolution, and most usually require a non-trivial experimental setup, including special hardware and software.

In this paper, we analyze the mechanism of magnetic contrast in defocused images, hereafter called as magnetic refraction, and show how the classical Fresnel imaging can be upgraded to the level of Lorentz phase microscopy. This combined method may be compared with other advanced magnetic imaging techniques in terms of resolution, simplicity, and the ability to quantitatively visualize local magnetic induction. Our approach is based on derivation of the magnetic transport-of-intensity equation (MTIE), and is illustrated with practical examples of magnetic induction mapping of patterned permalloy and Co islands as well as Nd–Fe–B hard magnets.

2. Theory

2.1. Intuitive description

The domain wall contrast in defocused images of magnetic materials has been well described in the classical work of Hirsch et al. [1] in terms of the Lorentz deflection angle (θ_L), experienced by the incident electrons passing through the magnetic sample. The typical value of the Lorentz angle is very small, $\theta_L \sim 10^{-5}$ rad, that is about 100 times less than typical Bragg diffraction angles in TEM ($\theta_B \sim 10^{-3}$ rad). Elementary wave consideration strongly suggests that the originally flat electron wave front experiences a local rotation upon exiting the sample surface by the same angle, θ_L, within magnetic domains, as schematically shown in Fig. 1c (right side). The local deflection of electrons will redistribute the observed intensity (Fig. 1e), forming a basis for the classical explanation of such a "magnetic" refraction effect. For comparison, in Fig. 1e (left side) we also show the intensity redistribution due to optical "light" refraction of the same beam by a non-magnetic sample. For simplicity, hereafter we shall use an approximation of small defocus, when the secondary effects of beam interference fringing at domain wall positions are not yet apparent. Because of the wave particle duality of electrons an alternative description to Lorentz deflection $\theta_L(\mathbf{r}, z)$ is the approach of wave front curvature mapping $\varphi(\mathbf{r}, z)$ (Fig. 1c). In general, this mapping will depend on the particular orientation of the domains within magnetic elements. For example, the electron-wave phase front for patterned magnetic elements shown in Fig. 1 is expected to be as presented in Fig. 2 due to the simultaneous contributions of optical and magnetic refraction components. In practice, the wave front curvature can be retrieved using holographic principles introduced by Gabor [8] for light optics. In the field of electron microscopy remarkable progress was achieved by the off-axis electron holography

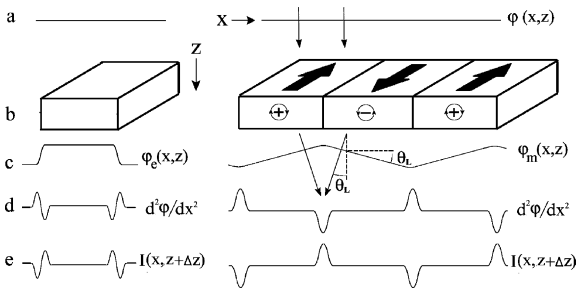

Fig. 1. Schematic diagram of the electron-beam deflection and wave front curvature due to scattering by non-magnetic (left side) and magnetic (right side) potentials of a sample imaged by Fresnel microscopy: (a) original flat front, (b) sample, (c) wave front at the exit plane, (d) second phase derivative as phase Laplacian, and (e) phase-contrast imaging $\partial I/\partial f$ approximated as intensity difference, recorded at zero and small defocus Δf value.

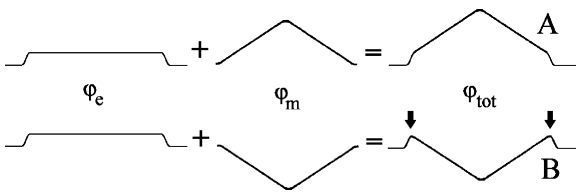

Fig. 2. Expected profiles of total phase map $\varphi_{tot}(\mathbf{r})$ for a magnetic sample, as shown in Fig. 1, due to contributions of electrostatic (φ_e) and magnetostatic (φ_m) phase shifts. The relative contributions to total phase shift depend on the shape of magnetic sample and, in particular, the magnetic domain structure. However, for most applications of magnetic-phase imaging, except for small nanoparticles, the electrostatic component is small and may be neglected (for details see the text).

(see for example [5,9,10]). However, this method requires highly coherent electron sources, while the noise and limited field of view of interferograms (typically, $\leqslant 1\,\mu m$ [9]) severely hampers its application over a larger scale.

On the other hand, a consideration by comparing the intensity difference $I(x, z+\Delta z) - I(x, z)$ at small defocus Δz (Fig. 1e) suggests that defocused intensity might be proportional in first approximation to the negative value of phase Laplacian (Fig. 1d). A similar idea was explored by Teaque in light optics, who suggested a non-interferometric approach to the phase-retrieval problem via solution of the so-called *transport-of-intensity equation* (TIE), based on intensity measurements at two closely spaced distances $I(\mathbf{r}, z)$ and $I(\mathbf{r}, z+\Delta z)$ [11]. Simultaneously, Van Dyck developed a similar approach for electron microscopy [12]. Later, several researchers examined this approach [13–17] in applications to optical refraction by non-magnetic objects. Meanwhile, a theoretical extension of the TIE concept for imaging magnetic materials was pessimistic [14], leading to the conclusion that magnetic induction (B) cannot be retrieved from the intensity measurements, except in special cases with non-vanishing intensity gradients $\nabla I \cdot (\mathbf{r}) \neq 0$, when "the product $\nabla I \cdot [\nabla \times \phi_V] \neq 0$", with the vector quantity $\nabla \times \phi_v$ identical to the vector potential $(e/c)\boldsymbol{A}$ [17]. However, this theoretical assessment does not logically agree with the experimental observations in Ref. [18] as well as our consideration of magnetic refraction (right side, Fig. 1). To reconcile the difference in theory, we examine the Aharonov–Bohm (AB) phase shift, which was not taken into account in Ref. [14] and not well clarified in Ref. [17], together with the continuity equation, and derive a new so-called MTIE suitable for most magnetic imaging applications. We note that most of our results can be directly compared with electron holography data [5,9,10].

2.2. MTIE and lorentz phase imaging

In this section, we derive the MTIE approach from first principles and show how the intensity measurements may be used for magnetic induction mapping in Lorentz phase microscopy.

Consider the stationary wave field describing the propagation of a monochromatic electron wave, $\psi = A\exp(ik_z z)$, with complex amplitude $A = a(\mathbf{r}, z)\exp[i\varphi(\mathbf{r}, z)]$ along the optical axis z of a TEM column. In a typical setting of Lorentz microscopy fast electrons with a total energy of $E = eU + m_0c^2$ (U: accelerating potential) interact with small magnetic objects above 50 nm size.

Here $\varphi(\mathbf{r}, z)$ is a small phase shift $\{|\varphi(\mathbf{r}, z)| \ll |k_z z|\}$ experienced by "free" electron wave at a distance z and position $\mathbf{r}(x, y)$ in a plane normal to the optical axis when moving with nominal phase $S = k_z z = (p_z/\hbar)z$ through the electromagnetic fields of the sample (Fig. 1). For free electrons, we also assume $k_z = 2\pi/\lambda$. Here m_0, p_z, k_z and λ are the rest mass, momentum, wave number, and wavelength of the electron, respectively. The motion of an almost-free electron wave obeys the relativistic time-independent Schrödinger equation with a solution known as the AB phase shift [19]. The information about sample fields is encoded in a phase shift $\varphi(\mathbf{r}, z)$ of the elastically scattered electron wave (phase $S_2 = k_z z + \varphi$) to be compared with a free electron "reference" wave (phase $S_1 = k_z z$) propagating far enough from the magnetic sample. At a certain distance z_0 away from the sample the electromagnetic potentials will vanish. Then, the AB solution for the phase shift $\varphi = S_2 - S_1$ at $z \to z_0$ is reduced to

$$\varphi(\mathbf{r}, z_0) = C_E \int_{-\infty}^{z_0} V(\mathbf{r}, z')\,dz' - \frac{e}{\hbar}\int_{-\infty}^{z_0} A_z(\mathbf{r}, z')\,dz', \quad (1)$$

where the value of the phase shift $\varphi(\mathrm{r},z)$ reaches its limit at $z \approx z_0$ ("exit wave" plane) and will not change for $z \geqslant z_0$, since both waves (S_1 and S_2) propagate further in a field-free space. The quantity $C_E(E) = \pi\gamma/\lambda U^*$, with γ and U^* as relativistic Lorentz factor and accelerating potential, respectively, is known as the interaction constant [10,22], which depends only on the electron energy (for 300 kV electrons, $C_E = 6.526 \times 10^{-3}$ rad/V nm), while V and A_z are the electrostatic and magnetostatic potentials integrated over the electron beam trajectory. For a field-free space, the continuity equation derived from the Schrödinger equation, yields the

conservation expression $(e\hbar/m)\nabla\cdot|a^2(\mathbf{r},z)\nabla S(\mathbf{r},z)|=0$ for current-density flow $\mathbf{j}=(e\hbar/m)a^2\nabla S$ (or current-probability flow $\mathbf{j}'=a^2\nabla S$) in field-free space. Both quantities, intensity $I=\Psi\Psi^*=a^2(\mathbf{r},z)$ and current density $\mathbf{j}(\mathbf{r},z)$, are observable and measurable quantum-mechanical parameters, sufficient, in principle, to reconstruct the object's phase shift. By taking into account the phase of scattered wave $S_2(\mathbf{r},z)=k_z z+\varphi(\mathbf{r},z)$ the continuity equation at $z\geqslant z_0$ yields

$$\nabla\cdot\{I(\mathbf{r},z)[\mathbf{n}_z k_z+\nabla\varphi(\mathbf{r},z_0)]\}=0, \tag{2a}$$

$$\nabla_\perp\cdot[I(\mathbf{r},z)\nabla_\perp\varphi(\mathbf{r},z_0)]=-k_z\partial I(\mathbf{r},z)/\partial z, \tag{2b}$$

where n_z is a unit vector along the beam's direction. In paraxial form, Eq. (2a) transforms to Eq. (2b) with gradient $\nabla_\perp$ operating only in the $\mathbf{r}(x,y)$ plane. Eq. (2b) is similar to the optical TIE-equation [11] and other continuity equations in physics [20]. However, the phase shift φ in Eq. (2b) now is well defined by the AB phase via Eq. (1). It agrees well with considerations in Fig. 1 and makes the MTIE approach different from the vector phases/potentials analyzed in the literature [14,15,17]. To obtain information about magnetic induction encoded in a phase shift, we consider the in-plane gradient from Eq. (1) as

$$\nabla_\perp\varphi=C_E\nabla_\perp\int_{-\infty}^{z_0}V\,\mathrm{d}z'-\frac{e}{\eta}\int_{-\infty}^{z_0}(\mathbf{n}_x\partial_x A_z+\mathbf{n}_y\partial_y A_z)\,\mathrm{d}z'. \tag{3}$$

The interaction constant $C_E(E)$ has a limiting value, $e/\hbar c$ for $E\gg m_0c^2$. The line z-path integrals in Eq. (3) at $z\geqslant z_0$ define the projected electrostatic potential and projected in-plane induction, and are only functions of $\mathbf{r}(x,y)$. Using the definition $\boldsymbol{B}(\mathbf{r},z')=\nabla\times\boldsymbol{A}_z(\mathbf{r},z')$ we denote these integrals as $tV_{\mathrm{in}}=\int V(\mathbf{r},z')\,\mathrm{d}z'$ and $t\mathbf{B}(\mathbf{r})=\int\mathbf{B}_\perp(\mathbf{r},z')\,\mathrm{d}z'$, and re-write Eq. (3) in another form

$$\nabla_\perp\varphi(\mathbf{r})=\nabla_\perp\varphi_{\mathrm{e}}+\nabla_\perp\varphi_{\mathrm{m}}=\sigma\nabla_\perp[tV_{\mathrm{in}}(\mathbf{r})]-\frac{e}{\hbar}[\mathbf{n}_z\times t\mathbf{B}(\mathbf{r})]. \tag{4}$$

Since both path integrals in Eq. (3) are finite, the variable t introduced in Eq. (4) may be considered as an effective sample thickness when the electromagnetic field is localized near the sample. Direct substitution of Eq. (4) into Eq. (2b) yields the most general form of the continuity equation

$$\nabla_\perp\cdot[I(\mathbf{r},z)\nabla_\perp\varphi_{\mathrm{e}}(\mathbf{r},z_0)]+\nabla_\perp\cdot[I(\mathbf{r},z)\nabla_\perp\varphi_{\mathrm{m}}(\mathbf{r},z_0)]=-k_z\partial I(\mathbf{r},z)/\partial z, \tag{5}$$

where the first and second terms represent, respectively, two independent mechanisms of optical (TIE) and magnetic (MTIE) refraction, as outlined in Fig. 1. The first term in Eq. (5), associated with the electrostatic field, tends to zero for samples of constant thickness and of uniform crystal potential. An estimate of the relative contributions to the AB phase shift indicates that the electrostatic component may only be significant for Lorentz phase imaging when cobalt or permalloy particle size is less than $\sim$40–60 nm. For patterned magnetic films, this term is expected to contribute only at the sharp sample edges (Fig. 1c, left side, and Fig. 2). Hence, by considering magnetic term as the major component of the total phase gradient in Eq. (4) and by temporarily neglecting the electrostatic term, we obtain the following first-order scalar equation:

$$\partial_y(I\cdot tB_x)-\partial_x(I\cdot tB_y)=\frac{\hbar k}{e}\cdot\frac{\partial I}{\partial z}, \tag{6}$$

which directly relates the defocused contrast, $\partial I/\partial z$, with in-plane components of projected magnetic induction $t\mathbf{B}(\mathbf{r})=\int\mathbf{B}_\perp(\mathbf{r},z')\,\mathrm{d}z'$ and, therefore, may be named as MTIE. We emphasize its similarity to the optical TIE; however, the mechanism of electron-wave refraction in Eq. (6) is due to magnetic properties of the sample. For Lorentz imaging the derivative $\partial I/\partial z$ can be replaced with $\partial I/\partial f$ ([22, Chapter 2]). At small defocus, $\Delta f\to 0$, it is approximated by the difference of two slightly defocused images $[I(\mathbf{r},+\Delta f)-I(\mathbf{r},-\Delta f)]/(2\Delta f)$, while $I(\mathbf{r},0)$ is an in-focus image. For better understanding of specific magnetic phase contrast Eq. (6) can be expressed [21] via the z component of vector equation:

$$e[I\nabla\times t\mathbf{B}+\nabla I\times t\mathbf{B}]_z=-\hbar k_z\partial I/\partial f. \tag{7}$$

Perhaps only the second term, $\nabla I\times t\mathbf{B}(\mathbf{r})$, was theoretically discussed in Ref. [14], leading to the conclusion that magnetic imaging based on intensity measurements is not feasible. Below, we show that this term is of minor importance in our

approach. Indeed, by re-writing Eq. (7) we obtain the following estimate:

$$[\mathrm{rot}\,\mathbf{B}(\mathbf{r})]_z = -\frac{\hbar k_z}{et}\frac{\partial I}{I\partial f} - [\nabla \mathrm{In}\, I \times \mathbf{B}(\mathbf{r})]_z \cong -\frac{2\Phi_0}{t\lambda}\frac{\partial I}{I\partial f}, \quad (8)$$

where the second term is small for uniform in-focus illumination and in many other practical cases. For a typical TEM experiment ($U = 300\,\mathrm{kV}$ and $t \approx 50\,\mathrm{nm}$), the pre-factor of the first term in Eq. (8), measured in Tesla, is very large ($\hbar k_z / |e| t = 2\Phi_0 / t\lambda = 4.136 \times 10^4$; $\Phi_0 = 2.068 \times 10^{-15}\,\mathrm{Wb}$ is a quantum of magnetic flux) compared to $|B| \leqslant 2.4\,\mathrm{T}$ for most magnetic compounds. The value of the in-plane gradient, $\nabla_\perp \ln I$, is small and agrees well with the Bouguer–Lambert–Beer's absorption law $\mathrm{In}[I(t)/I_0] = -\mu t$ with μ as the absorption coefficient. Hence, the second term in Eq. (8) may be neglected in foils of constant thickness and/or far enough from the sample's sharp edges when $\nabla_\perp \ln I \approx 0$. In accordance with Eq. (8), the remaining term $[\mathrm{rot}\,\mathbf{B}(\mathbf{r})]_z$ will produce a strong intensity contrast in defocused images of magnetic materials only in the areas of significant magnetization curling. For example, for magnetic vortices, either a very bright or dark dot contrast is experimentally observed (Fig. 3a), depending on the direction of vortex circulation. This first term is also responsible for the out-of-focus intensity contrast of domain walls, cross-tie walls, and for ripple contrast in Fresnel imaging [2,23] of magnetic films. The second term is important for the non-solenoidal induction, related, for example, to external field. Several examples of vortices imaging are discussed below.

2.3. Solution of MTIE/TIE equations

By introducing the new variables $X = (e/\hbar) \cdot tB_y$ and $Y = -(e/\hbar) \cdot tB_x$ in Eq. (7) and using $\mathrm{div}\,\mathbf{B} = 0$ we obtain

$$\partial_x(I \cdot X) + \partial_y(I \cdot Y) = -k \cdot \partial I/\partial z, \quad (9a)$$

$$\partial_x Y - \partial_y X = 0. \quad (9b)$$

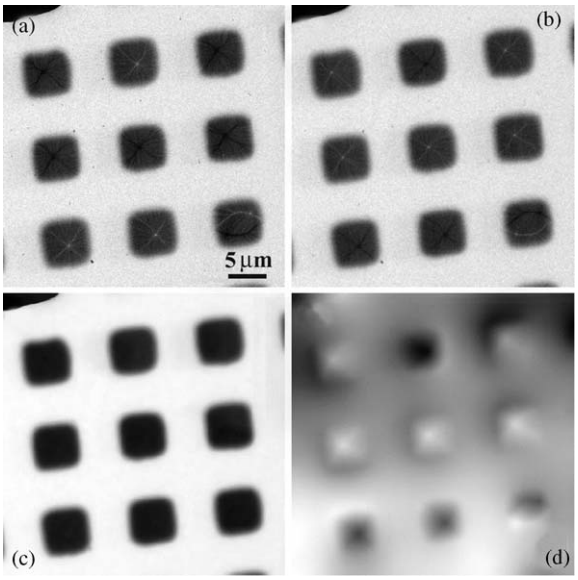

Fig. 3. The in situ Fresnel imaging of magnetic Co islands of approximately 7 μm size, patterned on a transparent Si_3N_4 membrane and recorded at $H = 0$ Oe: (a) under-focus, (b) over-focus, and (c) in-focus images recorded for the same elements. The image in (d) shows the map of recovered electron-wave phase shifts $\varphi(\mathrm{r})$ using the MTIE approach. The defocus step was $\Delta f \approx 150\,\mu\mathrm{m}$.

In principle, Eqs. (9a)–(9b) with known boundary conditions can be solved by the methods of differential calculus; however, this is not a trivial task in the general case of an arbitrary variable function $I(\mathbf{r}) > 0$. By using a vector function for the magnetic component $\nabla\varphi_\mathrm{m}(\mathbf{r}) = X(\mathbf{r})\mathbf{n}_x + Y(\mathbf{r})\mathbf{n}_y$ we make sure from Eq. (9b) that φ_m is differentiable. Then Eq. (9a) transforms into a standard continuity equation in paraxial form

$$\nabla_\perp \cdot (I\nabla_\perp \varphi_\mathrm{m}) = -k \cdot \partial I/\partial z. \quad (10)$$

To solve Eq. (10) an empirical variable $\nabla\psi = I\nabla\varphi$ [11,14] might be used to convert it to a Poisson equation $\nabla(\nabla\psi) = \nabla^2\psi = -k_z\partial I/\partial z$, followed by applying well-known algorithms for solving the Poisson equation. However, in our opinion, this approach may fail in the general case of magnetic imaging for the following reasons. First, the condition $\psi''_{xy} = \psi''_{yx}$, required by the Poisson equation, along with $\varphi''_{xy} = \varphi''_{yx}$, gives a hidden constraint $\varphi'_x(\mathbf{r}) \cdot I'_y(\mathbf{r}) = \varphi'_y(\mathbf{r}) \cdot I'_x(\mathbf{r})$ at every point of possible $\varphi(\mathbf{r})$-solution. Second, by

forcing the condition $\nabla\psi = I\nabla\varphi$ it is necessary to postulate that the vector field $I\nabla\varphi$ must be potential and irrotational, since $\mathrm{rot}(I\nabla\varphi) = \mathrm{rot}(\nabla\psi) \equiv 0$. This will require additional hidden constraints with no clear physical sense. On the other hand, in a general 3D-case, the vector field $\nabla\psi = I\nabla\varphi$ must be solenoidal, since $\mathrm{div}(I\nabla\varphi) = 0$. We note that these postulates were little discussed in the literature; nevertheless, several researchers (for example, Refs. [11,14,18,22]) used them for solving the phase-recovery problem. Meanwhile, this makes clear sense only for light refraction on the basis of physical assumptions, as used for the most recent optical phase retrieval in Ref. [24]. To bypass this theoretical difficulty, for magnetic imaging we suggest another general way of solving continuity equations with variable function $I(\mathbf{r}) > 0$. Since there is no analytical solution for Eqs. (9) and (10) with variable $I(\mathbf{r})$, we take advantage of fast Fourier methods. Knowing that the function $\varphi_m(r)$ is differentiable and $\varphi''_{xy} = \varphi''_{yx}$, by re-writing Eq. (10) in Poisson-like form

$$-\nabla_\perp^2 \varphi_m = k_z \partial_z \ln I + \nabla_\perp \varphi_m \cdot \nabla_\perp \ln I, \quad (I > 0) \tag{11}$$

we obtain the following integral solution:

$$\varphi_m(\mathbf{r}) = -\nabla_\perp^{-2}[k_z \partial_z \ln I + \nabla_\perp \varphi_m \cdot \nabla_\perp \ln I], \tag{12}$$

where the double integration by the inverse Laplacian operator $\nabla_\perp^{-2}$ can be performed by any appropriate method using the expression in brackets as the scalar image source. Unique phase-solution of Eqs. (11)–(12) up to some arbitrary constant can be obtained, for example, by the Fourier transform using the Neumann boundary condition [25]. When the second term in Eqs. (11)–(12) is small, as discussed for the $\nabla I \times t\mathbf{B}(\mathbf{r})$ term in Eqs. (7)–(8), the solution is obtained in one step as

$$\varphi_m(\mathbf{r}) = F^{-1}\{F[k_z \partial_z \ln I]/\mathbf{k}_\perp^2\}, \quad \mathbf{k}_\perp \neq 0, \tag{13}$$

where F and F^{-1} define the forward- and inverse-Fourier transforms for the image source given in brackets, and $\mathbf{k}_\perp$ is a frequency vector in Fourier space. The second small gradient-term can be included in the refined solution φ_m by iterating Eqs. (12)–(13) with the modified image source in Eq. (13) from Eq. (12). The solution converges in a few iterations and does not greatly differ from a simple one-step solution (13). Finally, the projected $t\mathbf{B}(\mathbf{r})$ map may be computed from Eq. (13) using relation (4) as

$$t\mathbf{B}(\mathbf{r}) = (\hbar/e)[\mathbf{n}_z \times \nabla_\perp \varphi_m] \tag{14}$$

We note that the structures of Eq. (10) and the more general Eq. (5) are essentially identical, while the solution by FT-method using Eqs. (12)–(13) does not impose any constraints except a reasonable Neumann boundary condition [25]. Hence, the total electron-wave phase shift $\varphi(\mathbf{r}) = \varphi_m(\mathbf{r}) + \varphi_e(\mathbf{r})$, using both MTIE and TIE approaches, can be retrieved essentially in the same way. For applications to magnetic materials, keeping in mind that the magnetostatic contribution usually is much larger than the electrostatic one, we recommend expressing phase gradients in terms of the projected induction $t\mathbf{B}(\mathbf{r})$ via Eq. (14) rather than by the simple phase gradient $\nabla_\perp \varphi(\mathbf{r})$. A more accurate separation of the potential contributions to the total phase is discussed below. The above results can be easily generalized for partially coherent electron waves [14].

This non-holographic approach for projected induction mapping in magnetic films is easy for practical implementation, while most of its results may be directly compared with the electron-holography data. For example, induction map (Fig. 4c), computed from a couple of defocused Fresnel images (Figs. 3a and b) recorded by CCD with 512×512 pixels, takes about 3–4 s for Dell-PC(500 MHz) computer, or 6–8 s for similar image of 1024×1024 pixel size. Note that the field of view in Fig. 3 is about $43 \times 43\,\mu m^2$, hence any retrieval of similar magnetic information from off-axis electron holograms of 1–5 μm size will require approximately $[43/(1-5)]^2 = 75$–1800 holograms, which is not practical.

3. Applications

3.1. In situ lorentz phase microscopy

Patterned 2D-arrays of magnetic polycrystalline permalloy and cobalt islands about 25–40 nm thick were grown on 30 nm thick silicon-nitride membranes supported on silicon wafers by means of

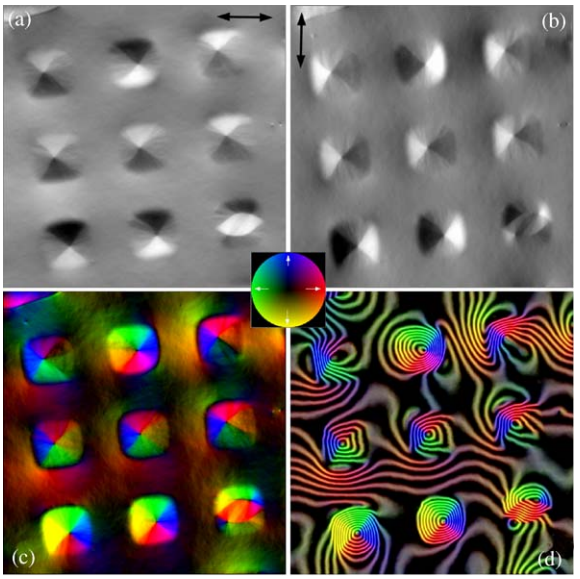

Fig. 4. The retrieved phase information, shown in Fig. 3d, was used to reconstruct separate tB_x (a) and tB_y (b) components of the projected magnetic induction $t\mathbf{B}(\mathbf{r})$, shown by color vector code (see inset) in the image (c) by neglecting with φ_e component. The image in (d) shows the distribution of magnetic flux, well approximated by the contours of equal phase shift, as proved by the analysis in Fig. 6.

electron-beam evaporation through a shadow mask in a UHV chamber. Shadow mask patterning allowed the growth of cobalt islands of $7 \times 7\,\mu m^2$ size ($\sim$49000 elements) with translation spacing of 14 μm in a single deposition step over an area of about 3 mm diameter. Our choice of samples was motivated by the need for a well-defined geometry of patterned arrays that are ideal for in situ Lorentz imaging and studies of magnetic switching phenomena. It also offers the possibility of separating magnetostatic and electrostatic potentials, and of clarifying the physics of magnetic interactions observed in experiments at the mesoscopic length scale. The samples were characterized by conventional TEM using a 300 keV microscope (JEM3000F). All Co-films had a grain size of about 10 nm and consisted of mixture of cubic and hexagonal closed-packed phases with isotropic properties over the film, which are known to be ferromagnetic. For in situ magnetizing experiments, Fresnel imaging and Lorentz phase imaging (see Section 2.2) were performed using the same magnetic field-calibrated JEM3000F microscope [26]. Since Co grains have random crystallographic orientation, magneto-crystalline anisotropy effects are expected to be weak [27] and general magnetization behavior versus applied field will be mostly determined by the shape-demagnetizing factors of the elements.

Figs. 3 and 5 show the typical results of an in situ magnetization experiment for Co islands 32 nm thick, as assessed by the EELS thickness measurement, and recorded at external fields $H = 0$ (Fig. 3) and 28 Oe (Fig. 5), respectively. Note that the magnetization ripple, usually observed at the demagnetization step ($H = 41 \to 14$ Oe), results in the nucleation of a vortex domain structure (Figs. 3a and b) at the lower field. Many more details (Figs. 4 and 5) about in-plane magnetization within the domain structure and the demagnetizing fields around the samples can be obtained by Lorentz phase imaging using the new MTIE approach. The phase, as shown in Fig. 3d, can be retrieved using Eqs. (11)–(14) discussed in Section 2.3. It provides much rich quantitative information. For example, just by visual inspection (Figs. 4 and 5) we conclude that the presence of magnetic vortices minimizes the leakage of magnetic fields from samples due to the formation of closure domains. On the other hand, the vortex domain structure remains quite mobile and easily follows the variations of the external field (Fig. 5) by the appropriate motion and deformation of domain walls. As a result, the hysteresis curve of 32 nm thick Co arrays, in general, remains rather narrow, reaching magnetic saturation at $|H| > 41$ Oe, in good agreement with the MFM data [28]. We note that with the help of non-holographic MTIE/TIE approach, the recovered phase (Fig 3d) may be compared with the electron-holography data, while the magnetic-induction components (Figs. 4a and b) with the appropriate data of the differential phase-contrast method [2] and Foucault imaging.

3.2. Separation of electrostatic and magnetostatic phase components

In this section we demonstrate a new practical way (Fig. 6) to separate the electrostatic (φ_e) and

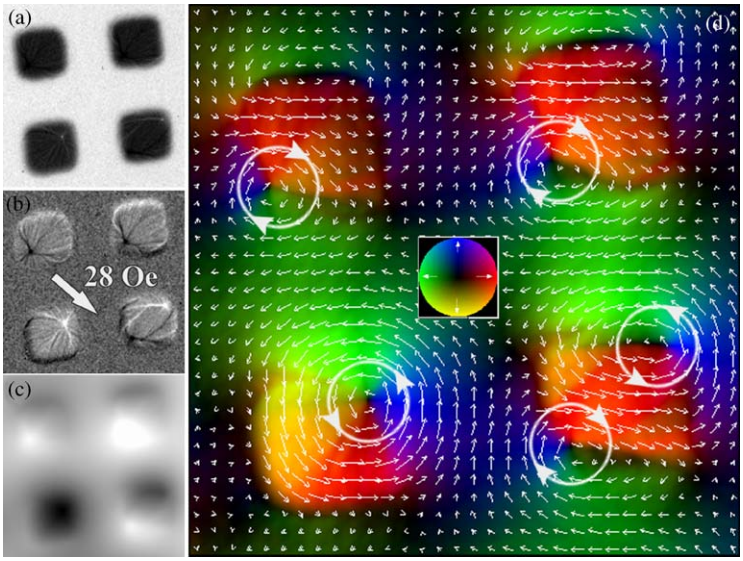

Fig. 5. Fresnel imaging of the same magnetic Co islands, as shown in Fig. 3, magnetized by in-plane field $H = 28$ Oe: (a) under-focus image, (b) $\Delta[\ln I(r)]/\Delta f$ gradient of intensity, and (c) recovered phase map for Co elements. The image in (d) shows the map of projected magnetic induction, presented both by color and vector code, as calculated from the electron-wave phase shift φ (c) using the MTIE approach. Note a cooperative wavy character of demagnetizing fields due to magnetization of Co islands along the direction of applied field marked by arrow in (b).

magnetostatic (φ_m) components of the total phase shift, based again on simple measurements of image intensity. This idea is based on the fact that the electrostatic phase is directly proportional to the sample's thickness according to the AB phase solution, Eq. (1). On the other hand, the in-focus intensity absorption contrast, such as shown in Fig. 3c, is also proportional to the sample thickness via the Bouguer–Lambert–Beer's absorption law (Section 2.2). Hence, by assuming that $\varphi_e(\mathbf{r}) \sim \ln[I_0/I(\mathbf{r})]$, with $I(\mathbf{r})$ being the recorded in-focus sample intensity, the magnetostatic component (Fig. 2) can be expressed as a function $\varphi_m(\mathbf{r}) = \varphi_{tot}(\mathbf{r}) - \varphi_e(\mathbf{r}) = \varphi_{tot}(\mathbf{r}) - C\ln[I_0/I(\mathbf{r})]$, where C is a fitting constant. The value of the constant C should be chosen to minimize most of the phase steps in $\varphi_m(\mathbf{r})$ map at the sharp sample edges; for example, such as those marked by arrows in Fig. 2 (images A and B). This can be done by constructing a fringe map as $\cos[N_m \cdot \varphi_m(\mathbf{r})] = \cos\{N_t \cdot \varphi_{tot}(\mathbf{r}) - N_e \cdot C \cdot \ln[I_0/I(\mathbf{r})]\}$, with $N_m = N_t = N_e = \text{const}$ as phase-amplification factors defining any suitable $2\pi/N$-phase resolution. Once such a constant C is found, and the "unknown" phase $\varphi_e(\mathbf{r}) = C \cdot \ln[I_0/I(\mathbf{r})]$ is subtracted, the remaining map appears to be pure magnetostatic phase $\varphi_m(\mathbf{r})$. This is illustrated in Fig. 6 by applying the phase separation process to the phase map shown in Fig. 3d. To quantitatively estimate the balance of the components in total phase, we suggest taking one more step. By adjusting the same density of fringes in the $\cos[N_e \cdot \varphi_e(\mathbf{r})]$ and $\cos[N_m \cdot \varphi_m(\mathbf{r})]$ maps with $N_e = 0.025-0.03$ and $N_m = 0.0005$ (Figs. 6a and b), we readily found that the ratio of $|\varphi_e|/|\varphi_m|$ contributions (Figs. 6c and d) is about $N_m/N_e = 0.0005/(0.025-0.03) = 0.017-0.020$, i.e. $\approx(1.7-2.0)\%$. Hence, the magnetic phase φ_m (Fig. 6d) contributes to the total phase as much as 98.0–98.3%. This result agrees well with a theoretical estimate for 32 nm-thick magnetic Co elements of 7 μm size: $|\varphi_e|/|\varphi_m| = (C_E \cdot V \cdot t)/[(e/\hbar) \cdot t \cdot B_\perp \cdot \Delta x)] = 0.0199$, i.e. $\approx 2.0\%$, under assumption of the following Co parameters: magnetic induction $B_{sat}(298\,\text{K}) = 1.78$ T; calculated inner potentials $V = 29.4$ (FCC structure) and 29.6 (HCP) Volts, using known $F_{0\,0\,0}$ electron structural factors [29]; and $\Delta x = 3.5$ μm, as follows from the geometry of magnetic vortices shown in Fig. 4.

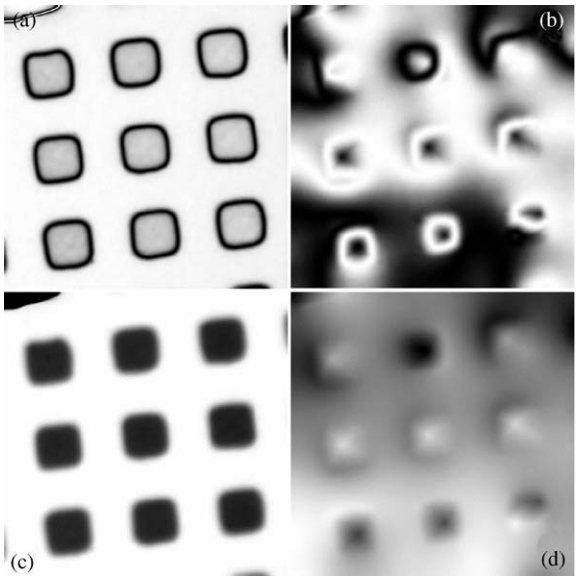

Fig. 6. Results of separating electrostatic (φ_e) and magnetostatic (φ_m) contributions to total phase shift using the phase map and in-focus image: (a) electrostatic phase as $\cos(N_e\varphi_e)$ with relative amplification factor $N_e = 0.025$, (b) magnetostatic phase as $\cos(N_m\varphi_m)$ with relative amplification factor $N_m = 0.0005$. Pure electrostatic (c) and magnetostatic (d) phases were separated using the procedure described in the text. Note that the relative phase contributions to total phase are inversely proportional to their relative amplification factors.

Note that the new phase-separation method described herein does not require any special knowledge about thickness, magnetic and/or electrostatic properties of sample. It generates fairly reliable results based on total phase map and in-focus image intensity, provided that sufficiently sharp thickness steps at the sample edges are available. It is also independent of the experimental defocus used to construct the intensity derivative $\Delta I(\mathbf{r})/\Delta f$. The above example of phase separation illustrates that magnetic Lorentz imaging, except for very small magnetic nanoparticles, in general is well described by the MTIE equation, while the electrostatic phase φ_e presented by the TIE term in the continuity Eq. (5) may be effectively neglected.

3.3. Phase microscopy of $Nd_2Fe_{14}B$ magnets

The above discussion on balance of magneto- and electrostatic contributions can be expanded to other cases of Lorentz magnetic imaging. Keeping in mind that magnetic phase φ_m is the major component in Eq. (5), we can use a semi-quantitative description for other magnetic objects of arbitrary shape and thickness, except, as mentioned earlier, small nanoparticles. For example, in Fig. 7a the defocused Fresnel image of a $Nd_2Fe_{14}B$ hard magnet was used to map the projected magnetization (Fig. 7b). The boundary-value problem was solved by the Neumann condition [25]. The image in Fig. 7a was recorded for a sample of unknown thickness. A non-desirable contribution of strong intensity variations, caused by the crystal foil banding (elastic scattering), and thickness variations (inelastic) close to the dynamic range of input CCD-signals, has been essentially compensated for the recovered phase by normalization of recorded images ($\Delta I/I$), as follows from the MTIE solution given by Eqs. (6), (8) and (12). Additional confirmation of the phase retrieval is obtained by comparing an independent experimental Foucault image (Fig. 7c) and the calculated one (Fig. 7d), derived from Fresnel image (Fig. 7a).

Note that practical implementation of this approach requires additional consideration of several questions related to the quality of recorded images. This may be related to (a) noise performance, dynamic range and pixel resolution of the CCD; (b) image drift, defocus, distortions, filtering and image alignment problems; and (c) new improvements of MTIE/TIE phase retrieval algorithm for digitally recorded images. Many of them related to noise and image alignment have been well addressed in Ref. [22, Chapter 5]. The others will be a subject for future improvements of the technique.

4. Conclusion

In conclusion, we have developed a method of Lorentz phase microscopy for magnetic materials, based on magnetic transport-of-intensity equation (MTIE). We found an appropriate solution of this equation. It was shown theoretically and experimentally that defocused Fresnel contrast in ferromagnets is caused by the local curling of magnetization about magnetic vortices and

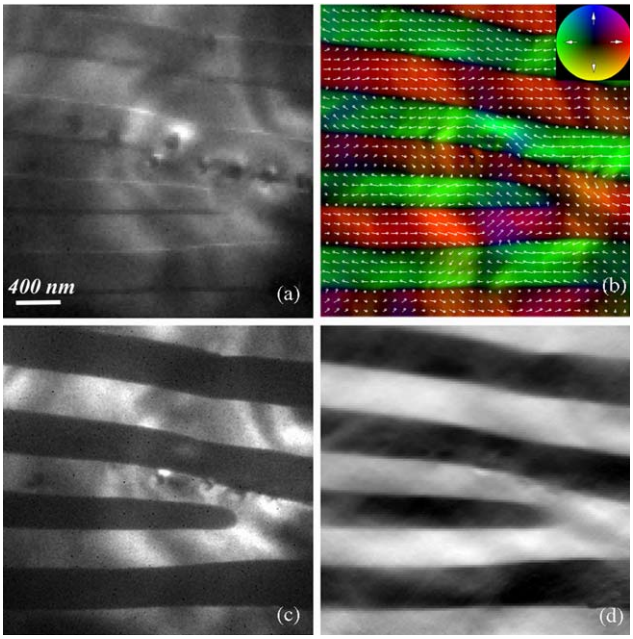

Fig. 7. Weak domain wall pinning by the dislocation pile-up at the low-angle grain boundary in $Nd_2Fe_{14}B$ magnet: (a) experimental defocused Fresnel image used for the reconstruction of projected induction vector map (b) with color inset encoding its amplitude and direction; the experimental Foucault image (c) may be compared with calculated projected $tB_x(\mathbf{r})$ component (d) derived from the image (a) using the MTIE approach.

domain walls. We also established an experimental way for the separation of phase components due to electrostatic and magnetostatic potentials contributing to total phase shift. Our approach is simple and, therefore, may be important for general understanding and practical use of non-holographic methods in the phase-retrieval problem, especially for quantitative magnetic imaging by Lorentz microscopy.

Acknowledgements

This work was supported by the US DOE, Division of Materials, Office of Basic Energy Science, Contract No. DE-AC02-98CH10886. The authors acknowledge M. Malac for providing the sample for Fig. 3.

References

[1] P.B. Hirsch, A. Howie, R.B. Nicholson, D.W. Pashley, M.J. Whelan, Electron Microscopy of Thin Crystals, Butterworths, London, 1965, pp. 392–416 (Chapter 16).
[2] J.N. Chapman, P.R. Aitchison, K.J. Kirk, S. McVitie, J. Appl. Phys. 83 (1998) 5321.
[3] J.B. Wedding, M. Li, G.-C. Wang, J. Magn. Magn. Mater. 204 (1999) 79.
[4] P. Grutter, H.J. Mamin, D. Rugar, Magnetic force microscopy, in: R. Wiesendanger, H.-J. Gunterodt (Eds.), Scanning Tunneling Microscopy II, Vol. 28, Springer, Berlin, 1992, pp. 151–207.
[5] A. Tonomura, Electron Holography, Springer, Berlin/Heidelberg, 1999.
[6] J. Unguris, D.T. Pierce, R.-J. Celotta, Rev. Sci. Instrum. 57 (1984) 1314.
[7] C.T. Chen, et al., Phys. Rev. Lett. 75 (1995) 152.
[8] D. Gabor, Nature (London) 161 (1948) 777.
[9] R.E. Dunin-Borkowski, M.R. McCartney, B. Kardynal, D.J. Smith, J. Appl. Phys. 84 (1998) 374.
[10] R.E. Dunin-Borkowski, M.R. McCartney, D.J. Smith, S.S.P. Parkin, Ultramicroscopy 74 (1998) 61.
[11] M.R. Teaque, J. Opt. Soc. Am. 73 (1983) 1434.
[12] D. Van Dyck, J. Microsc. 132 (1983) 31;
D. Van Dyck, W. Coene, Optik 77 (1987) 125;
D. Van Dyck, M. Op de Beeck, W. Coene, Optik 93 (1993) 103.
[13] A. Snigirev, I. Snigireva, V.G. Kohn, S. Kuznetsov, I. Schelokov, Rev. Sci. Instrum. 66 (1995) 5486.
[14] D. Paganin, K.A. Nugent, Phys. Rev. Lett. 80 (1998) 2586.

[15] T.E. Gureev, K.A. Nugent, J. Opt. Soc. Am. A13 (1996) 1670;
T.E. Gureev, A. Roberts, K.A. Nugent, J. Opt. Soc. Am. A12 (1995) 1942.
[16] K.A. Nugent, T.E. Gureev, D.F. Cookson, D. Paganin, Z. Barnea, Phys. Rev. Lett. 77 (1996) 2961.
[17] K.A. Nugent, D. Paganin, Phys. Rev. A 61 (2000) 063614.
[18] S. Bajt, A. Barty, K.A. Nugent, M. McCartney, M. Wall, D. Paganin, Ultramicroscopy 83 (2000) 67.
[19] Y. Aharonov, D. Bohm, Phys. Rev. 115 (1959) 485.
[20] S. Chikazumi, Physics of Magnetism, R.E. Krieger Publishing Co., Malabar, FL, 554pp.
[21] V.V. Volkov, Y. Zhu, Phys. Rev. Lett. 91 (2003) 043904.
[22] M. DeGraef, Y. Zhu (Eds.), Magnetic imaging and its applications to materials, Experimental Methods in the Physical Sciences, Vol. 36, 2001, Academic Press, New York (Chapter 2, p. 40; Chapter 5, p. 143).
[23] V.V. Volkov, Y. Zhu, Philos. Mag. (2003), accepted for publication.
[24] D. Paganin, S.C. Mayo, T.E. Gureev, P.R. Miller, S.W. Wilkins, J. Microsc. 206 (2002) 33.
[25] V.V. Volkov, Y. Zhu, M. De Graef, Micron 33 (2002) 411.
[26] V.V. Volkov, D.C. Crew, Y. Zhu, L.H. Lewis, Rev. Sci. Instrum. 73 (2002) 2298.
[27] S.X. Zhou, Y.G. Wang, J.H. Ulvensoen, R. Hoier, IEEE Trans. Magn. 30 (1994) 4815.
[28] M. Löhndorf, A. Wadas, R. Wiesendanger, Appl. Phys. A 65 (1997) 511.
[29] D. Rez, P. Rez, I. Grant, Acta Cryst. A 50 (1994) 481.